ELSEVIER

Contents lists available at ScienceDirect

Journal of Alloys and Compounds

journal homepage: www.elsevier.com/locate/jalcom





Morphology evolution of plate-like precipitates in a polycrystalline Ni-based superalloy

Parisa Darvishmotevally ^a, Mohammad Saadati ^a, Jonathan Cormier ^b, Mohammad Jahazi ^a, ^a

- ^a Mechanical Engineering Department, École de Technologie Supérieure (ÉTS), 1100 Notre-Dame West, Montreal, QC H3C 1K3, Canada
- b Institut Pprime, UPR CNRS 3346, Physics and Mechanics of Materials Department, ISAE-ENSMA, 1 avenue Clément Ader, BP 40109, Futuroscope, Chasseneuil Cedex 86961, France

ARTICLE INFO

Keywords:
Interfaces
Nucleation
Growth
Morphology
Polycrystalline Ni-based superalloy

ABSTRACT

The formation of a dendrite arm-like interface, called protrusions, between plate-like precipitates and the surrounding matrix was studied in AD730TM Ni-based superalloy. The evolution in the morphology and reprecipitation sequence of γ' particles after solution heat treatment has been investigated using Electron Backscatter Diffraction (EBSD), Field Emission Scanning Electron Microscopy (FE-SEM), Transmission Electron Microscopy (TEM), and Energy-Dispersive Spectroscopy (EDS). For the first time, atomic-scale investigations using High-Resolution Transmission Electron Microscopy (HR-TEM) revealed that protrusions tend to nucleate on the facet interface of the existing plate-like particles with a high coherency to the matrix. An analysis based on the application of the Brook equation was conducted, and a correlation was established between the frequency of protrusions and dislocation spacing, supporting the proposed dislocation-driven nucleation mechanism. TEM analysis revealed a gradient in chemical composition at the matrix-protrusion interface, which and analyzed in the framework of the dissolution and growth theories of precipitates. The results indicated that the protrusion occurred in a growth process during cooling, leading to the depletion of the main precipitating elements in the matrix in the adjacent zones. Using diffusion theory, element-specific diffusion behavior was analyzed, and it was revealed that Nb diffusion plays a critical role in protrusion evolution and governs the depletion of γ' -forming elements (Ni, Al, Ti, Nb) near the interface. The precipitation sequence and composition are analyzed in terms of the diffusion of γ' -forming elements. The evolution in the chemical composition of different precipitates indicated that the protrusions form after the precipitation of plate-like γ ' and before that of secondary γ ' on plate-like precipitates with about 0.27 % misfit. Based on the obtained results, it was concluded that the formation mechanism of protrusions is nucleation on misfit dislocations at the precipitate-matrix interface, and growth on {111} facet planes of plate-like precipitates. Additionally, the level of matrix supersaturation controls their growth kinetics.

1. Introduction

The exceptional strength of wrought Ni-based superalloys primarily stems from the γ ' precipitates with an L1_z structure [1,2]. Additionally, solid-solution strengthening provided by alloying elements, such as Cr, Co, Fe, Ti, Nb, Al, W, and Mo within the matrix, further enhances the overall performance of these superalloys [3,4]. Carbides at grain boundaries enhance creep resistance by restricting grain boundary sliding at elevated temperatures [1,5,6]. Cr and Al elements provide corrosion resistance through the formation of protective Cr_2O_3 and Al_2O_3 films [7,8]. They are used for blades, disks, and other critical

applications in aircraft engines and industrial gas turbines [9,10]. The mechanical properties of superalloys are notably influenced by microstructural factors in the matrix as a result of dislocation density which affects recovery, recrystallization, and grain growth [11–13]. Additionally, the mechanical properties are significantly influenced by the size, composition, volume fraction, and morphology of second-phase particles, such as different types of γ precipitates and carbides, etc. [14–16].

A wrought Ni-based superalloy can display a variety of second-phase particle morphologies, including spheres, cubes, plates, octets of cubes, rafts, etc. [14,15]. The changes in morphology are believed to be

E-mail address: Mohammad.jahazi@etsmtl.ca (M. Jahazi).

^{*} Corresponding author.

influenced by the combined effects of elastic strain energy, interface energy, and elastic interaction energy [15,17,18]. In the case of Ni-based superalloys, the elastic strain energy at the interface, which manifests itself in the lattice misfit (δ), has been reported to be the most important factor [18–20]. Their lattice parameters and δ are known as the alloy-dependent parameter [17,21–23]. Therefore, the interphase interface plays a crucial role in determining the second phase's morphology [15,18,24]. In addition to the chemical composition, evidence has been presented that γ ' morphology is also influenced by kinetic factors, such as the cooling rate [20,25,26].

The Smith–Zener model predicts that this precipitate usually pins boundary migration and therefore limits grain growth during sub-solvus forging and heat treatment [27,28]. The primary γ ' serves not only to anchor grain boundaries but also to trigger recrystallization through the reverse precipitation of the γ phase, which takes place before deformation at the periphery of the primary γ '. During this transformation, a coherent shell forms around the primary precipitate (completely or partially) [29]. As a result, the nucleus grows when its surroundings differ in stored energy, transforming into recrystallized grains that are coherent with their precipitates [29–31].

Vernier et al. [32,33] recently reported a novel interaction between these close-to-coherent primary y' precipitates and their host recrystallized grain. They discussed that this interaction led to plate-like shape precipitates with {111} facets on the recrystallization front in some Ni-based superalloys with low γ - γ ' lattice-mismatch. It is well known that a new phase tends to precipitate from the matrix, it preferentially nucleates at the close-packed planes of the matrix to minimize the interface energy between the precipitate and matrix [34]. Moreover, the twin boundaries, alongside boundaries, are considered the most favorable sites for precipitation due to their associated lattice energy [35]. The close-packed planes and twin boundaries often manifest as flat segments oriented in {111} planes in face-centered cubic (FCC) structures of matrix [24,36]. So, the {111} planes as a chosen plane are more preferred for their nucleation in FCC material. The differences in size, shape, and orientation range in contrast to the precipitates in the recovered grain indicated that their formation is not simply due to direct bypass by the recrystallization front. These precipitates extend onto {111} facets, a result of the crystallographic structure of the recrystallization front and its direct growth with {111} facets on a recrystallized grain. They are known as T/C-type precipitates [32,33]. These precipitates form boundaries over <111> directions with specific rotation angles (about 60 degrees for T type and almost 0 degrees for C type) to minimize their interfacial energy not only on the recrystallized side but also on the recovered side. The low interfacial energy of the two surfaces of the T/C-type precipitates is energetically less demanding to be bypassed with grain boundaries. Consequently, recrystallized grains expand towards the recovered grains containing a high density of semi-coherent precipitates, leading to unconventional orientations and morphologies of the γ '-precipitates [32,33]. The coexistence of T/C-type precipitates in some nickel-based polycrystalline superalloys implies that the mechanism described could apply to a wider range of materials with low magnitude lattice misfits [32]. In addition to Ni-based superalloys, Shanmugam et al. [37] investigated Al₃(Sc, Zr, Ti) nanoparticles in an annealed cold-rolled aluminum alloy. Their findings revealed that these nanoparticles formed semi-coherent twin interfaces on their shorter facets, while the longer facets exhibited coherent (111) twin-type interfaces with the matrix. Although the interface characteristics of cuboidal precipitates have been widely investigated and quantitatively discussed in single-crystal Ni-based superalloys [31,38,39], research and discussion on the evolution of the new semi-coherent plate-like γ' morphology have been quite limited in polycrystalline Ni-based superalloys.

Hence, this research aims to investigate the combined effects of interface characteristics and local chemical composition on the evolution of plate-like γ' morphology after solution heat treatment. A detailed analysis using scanning and transmission electron microscopy

techniques reveals a novel interface structure in the AD730 $^{\rm IM}$ Ni-based superalloy. Based on these findings, a nucleation and growth mechanism is proposed, governed by misfit dislocation spacing and elemental diffusion gradients. In particular, the proposed mechanism is based on the analysis of the semi-coherent interfaces that exhibit the plate-like precipitates with T/C-type orientation, which results in misfit accommodation through dislocation networks. The latter acts as a preferential site for the nucleation of the observed protrusions. In contrast, other precipitates, such as primary, secondary, and tertiary γ' , either lack sufficient alloying elements for reprecipitation or form coherent interfaces without dislocations, making it less favourable for the formation of protrusions at their boundaries. Based on these findings, a nucleation and growth mechanism is proposed, governed by misfit dislocation spacing and elemental diffusion gradients.

2. Experimental

The material used in the present investigation was a Ni-based superalloy with the following chemical composition: Ni-15.7 Cr-8.5 Co-4 Fe-3.1 Mo-2.25 Al-2.7 W-3.4 Ti-1.1 Nb-0.015 C-0.01 B, and 0.03Zr (wt %) [40]. A forged AD730TM bar provided by Aubert & Duval Co. was heat-treated after forging with a solution at 1080° C for 4 h, followed by air cooling ($10-20^{\circ}$ C/s).

The solutionized-treated bars were sectioned using wire electrodischarge machining (EDM) and subsequently prepared via standard metallographic techniques. Finally, the surface was subjected to chemomechanical polishing with 50 nm diameter colloidal silica using a Buehler VibroMet™ polisher. To characterize the interfaces between the matrix and the precipitates, the Hitachi IM4000Plus ion milling system was used for 20 min to remove remaining fine scratches and deformed surfaces. During ion milling, a low rotation speed (25 rpm) was used under the Ar ion gun, with the accelerating voltage set to 5 kV. The inclination or milling angle of the sample surface to the horizontal was set to 10°. This method was specifically developed to analyze the protrusions at the interface between the matrix and certain precipitates since the conventional etching techniques cannot be successfully applied to reveal such details due to the local attack on interfaces. Ion milling enhances chemical and channeling contrast in SEM imaging, allowing observation in an as-polished state without chemical etching. Bruker FlatQuad EDS detectors and the Bruker e Flash HR Electron Backscatter Diffraction (EBSD) detector were used in the Hitachi SU-8230 cold FESEM for chemical analysis and misorientation analysis. To illustrate grain evolution, EBSD imaging was performed at low magnification (x150) with an imaging area of 591 \times 845 μ m² and a step size of 1.1 μ m. Intragranular examinations were conducted with a smaller imaging area of 50.7 \times 35.3 μ m² using a step size of 67 nm at 2.5 Kx magnification. EBSD analysis was performed using the ESPRIT 2.6 software package, developed by Bruker, and MTEX. This software was used to analyze both the average misorientation and the Inverse Pole Figure (IPF) maps. In the IPFY map, the Y direction represents the vertical direction of the images.

Mechanical grinding was used to prepare thin films of 1 mm thickness for transmission electron microscopy (TEM) investigations. High energy (30 kV) gallium ions were used to prepare lamellae with a thickness of 150 nm using a Hitachi FB-2000A Focused Ion Beam (FIB). The microstructural observations were performed using a JEOL JEM/F200 TEM set to operate at 200 kV. The lamellae were then further thinned with a Thermo Scientific Helios 5 Hydra UX Dual Beam (30 kV) using a 90 pA current until a thickness of 70 nm. This thin film sample allows precise Energy dispersive spectroscopy (EDS) compositional analysis of precipitates approaching the thickness of the film [41] and high-resolution transmission electron microscopy (HR-TEM) analysis. For the analysis of the TEM results, DigitalMicrograph version 3.60.4435.0 was employed.

3. Results and discussion

Fig. 1a shows the presence of different size distributions of precipitates in the matrix. In an earlier study on this material, it has been shown that the large-size primary particles are partially dissolved during the solution treatment and remain as large-size blocks after cooling to room temperature [40,42]. In contrast, during cooling to room temperature, much smaller newly formed particles nucleate throughout the matrix [20,43]. In multiphase systems, only a few particles will nucleate at higher temperatures, mainly due to slight undercooling below the γ '-solvus temperature (secondary γ '). Under these conditions, γ -matrix regions far from these particles are supersaturated during decreasing temperatures [20,44]. As the temperature decreases further, supersaturation increases, allowing new nucleation to burst between the previous precipitates, as illustrated in Fig. 1b [20,43]. The formation of these cooling-induced γ '-particles initiates a decrease in the supersaturation level of the solute elements. Once the third γ ' population nucleates, most of the saturation is used up, and the matrix reaches stability [23].

Fig. 1b also highlights γ ' precipitates, which exhibit a nearly plate-like morphology, a characteristic that has been previously reported in wrought low-lattice mismatch Ni-based superalloys [32,33]. The plate-like precipitate is found predominantly in recrystallized grains, which have significantly grown into the surrounding recovered grains. The plate-like precipitates in the sample section, combined with the development of protrusions (white arrows), suggest a complex interplay between the lattice mismatch, local compositional changes, and the mechanism of γ ' phase growth. This unique microstructural feature will be examined further through detailed characterization techniques to elucidate its formation mechanism.

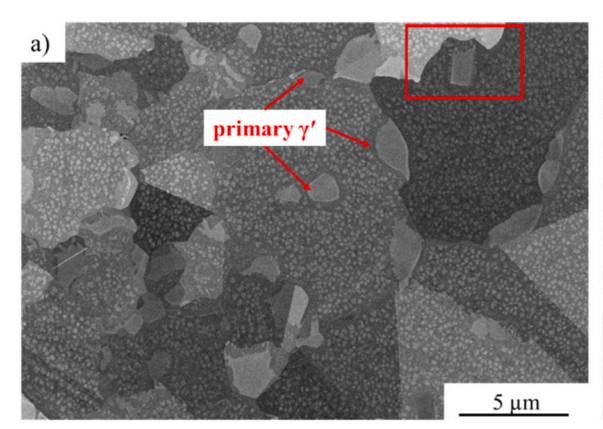
3.1. Plate-like γ ' precipitates

In this study, Plate-like precipitates were directly observed in the asreceived Ni-base superalloy. These findings align with those reported by Vernier et al. [32,33], on AD730TM, René65, and PER72 alloys, confirming the presence of such facets in similar alloy systems. The microstructure of the samples exhibits significant heterogeneity, as illustrated in Fig. 2, with the coexistence of equiaxed recrystallized and elongated non-recrystallized grains. In Fig. 2a-b, the IPF map and grain average misorientation map indicate that the microstructure exhibited a wide range of grain sizes, as a result of partial recrystallization. This map is instrumental for distinguishing between small recrystallized grains (\sim 20 μ m), large recrystallized grains (\sim 60 μ m), and non-recrystallized grains. The distinction between recrystallized and non-recrystallized regions was determined using the grain average misorientation (GAM) map. Grains exhibiting a misorientation of less than 2° were classified as

recrystallized, whereas those with misorientation values exceeding 2° were considered non-recrystallized [45]. Significantly larger recrystallized grains are observed near non-recrystallized elongated grains, while in other areas, much smaller equiaxed recrystallized grains are present. Both small and large recrystallized grains may have nucleated during sub-solvus forging [36]. However, during the solution treatment, only some of these grains experience significant growth, driven by differences in stored energy and boundary mobility [46]. As described by Vernier et al. [32], the large recrystallized grains, which expand into adjacent recovered grains, share a <111> axis with them and contain C/T-type precipitates [32,33,47].

Higher magnification analysis of the white-boxed region in Fig. 2a is presented in Fig. 3a–c, depicting small equiaxed grains with plate-like γ ' precipitates. Fig. 3a and b present the micrograph and EBSD-IPFY map corresponding to the white-boxed region in Fig. 2. Based on the IPFY contrast and grain morphology, this area is identified as recrystallized. High-magnification imaging in Fig. 3c reveals the presence of protrusions on the plate-like γ' precipitates, indicating localized reprecipitation behavior. Most primary precipitates are located at triple junctions and grain boundaries [40,42], lacking an orientation relationship with the surrounding matrix grains [1,33]. Charpagne et al. [48] studied precipitates in a René 65 superalloy and found large precipitates (multiple micrometers in diameter) to be coherent with their matrix grains. This result was unexpected because the matrix was coherent with such large particles, despite an apparent reason for it [1,33]. A later study by Vernier et al. [32,33] showed similar interfaces with {111} facets at recrystallization fronts in three Ni-based superalloys. Precipitates in this matrix are found to be slightly misoriented by a few degrees or close to twin orientation relationships. Based on the above analysis, it can be concluded that there are some micrometric plate-like precipitates with {111} facet on the side of recrystallized grains that have a specific orientation (about 60° or 0°) with the surrounding matrix after the forging process.

The micrograph, IPFY map, and point-to-point disorientation values of these plate-like precipitates are reported in Fig. 4. In Fig. 4a, plate-like precipitates with protrusions are shown, with the protrusions becoming more visible in the higher-magnification image in the left corner. The point-to-point disorientation is analyzed along arrows 1–4 (marked in Fig. 4b) traversing through the matrix and the plate-like γ precipitates as shown in Fig. 4c-d. In Fig. 4b, additional plate-like precipitates are indicated by white arrows. Among these, two representative precipitates were selected for detailed microstructural characterization. Specifically, in Fig. 4c, a high point-to-point disorientation value is observed at the interface of the matrix/ plate-like precipitate and plate-like precipitate/ matrix across lines 1 and 2. The point-to-point disorientation remains about 60 degrees, which is the typical angular orientation for a twin



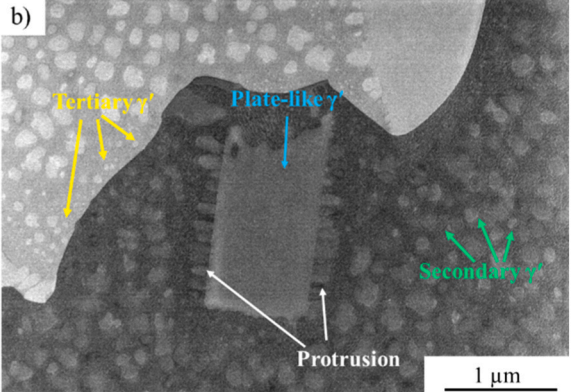


Fig. 1. Secondary electron (SE) micrograph showing the microstructure of a sample after a post-forging heat treatment involving solution for 4 h at 1080 °C and air cooling(10–20 °C/s) (a) primary γ ' precipitates are indicated by red arrows. (b) enlarged view of the red box in (a), showing secondary γ ' (green arrows), tertiary γ ' (yellow arrows), plate-like γ ' (blue arrow), and protrusions (white arrows).

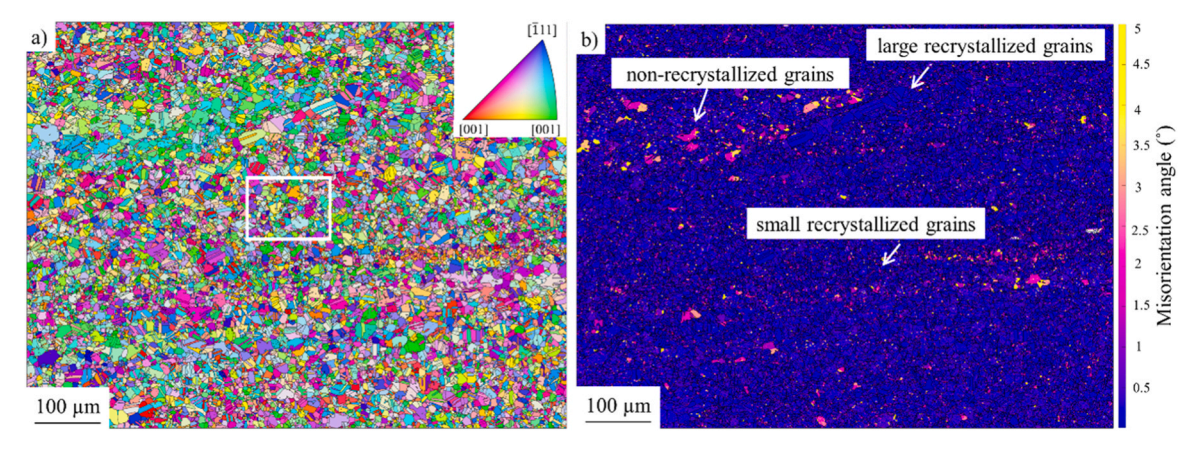


Fig. 2. Microstructure of AD730 $^{\text{TM}}$ samples containing small recrystallized grains, large recrystallized grains, and non-recrystallized grains, (a) an EBSD-IPFY map overlayed with colors representative of the IPF color code, (b) a misorientation map with three distinct grain populations indicated.

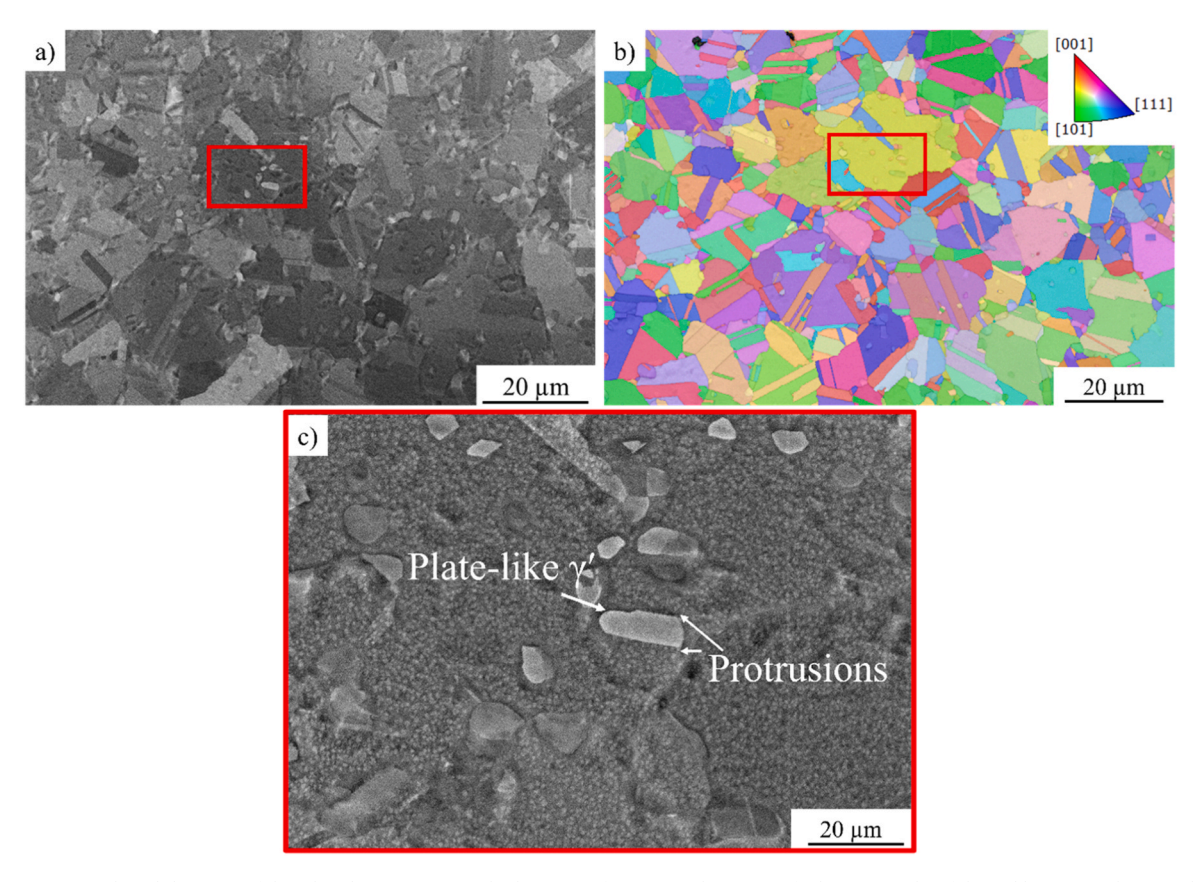


Fig. 3. (a) SE micrograph and (b) EBSD of the white box in Fig. 2a at higher magnification, and (c) magnified micrographs of the red box in (a) showing the plate-like precipitation with protrusions in small recrystallized grain.

boundary (Yellow arrowed precipitates in Fig. 4a) [33,37]. As mentioned before, this type of precipitate was identified as T-type and this high-value misorientation at the precipitate-matrix interface is possibly due to rotation during recrystallization [33]. Conversely, as reported in Fig. 4d, point-to-point disorientation values across lines 3 and 4 are near zero, indicating minimal crystal rotation in these precipitates (called C-type precipitates). C-type precipitates exhibit a misorientation of a few degrees relative to the matrix (Red arrowed precipitates in Fig. 4a) [32,33].

Fig. 5 exhibits the presence of an intergranular precipitate that resembles a T-type or C-type plate-like precipitate. It has a semi-spherical appearance and a single-faceted side with protrusions. Fig. 5b—h show this precipitate and its protrusions are enriched in the gamma prime

forming elements (Ni, Al, Ti, Nb) [49].

Fig. 6a displays a dark-field TEM image of a γ' precipitate with protrusions, alongside SAED patterns, to analyze the structural features and orientation relationships at the γ/γ' interfaces. The images were captured along the <011> zone axis, applicable to both the matrix and the γ' precipitate. To investigate the crystallographic structure and correlations, the SAED patterns of 1–8 marked by white circles were acquired by gradual movement from precipitate to protrusion, twined region, and matrix. The $\{200\}$ and $\{111\}$ reflections on SAED 1 and 8, were acquired from γ and γ' precipitate. In Fig. 6b and j, SAED 1 in [011] and [112] zone axes confirm the ordered L12 structure of the γ' phase, with additional $\{100\}$ and $\{011\}$ superlattice reflections highlighted by red circles [1,37,50,51].

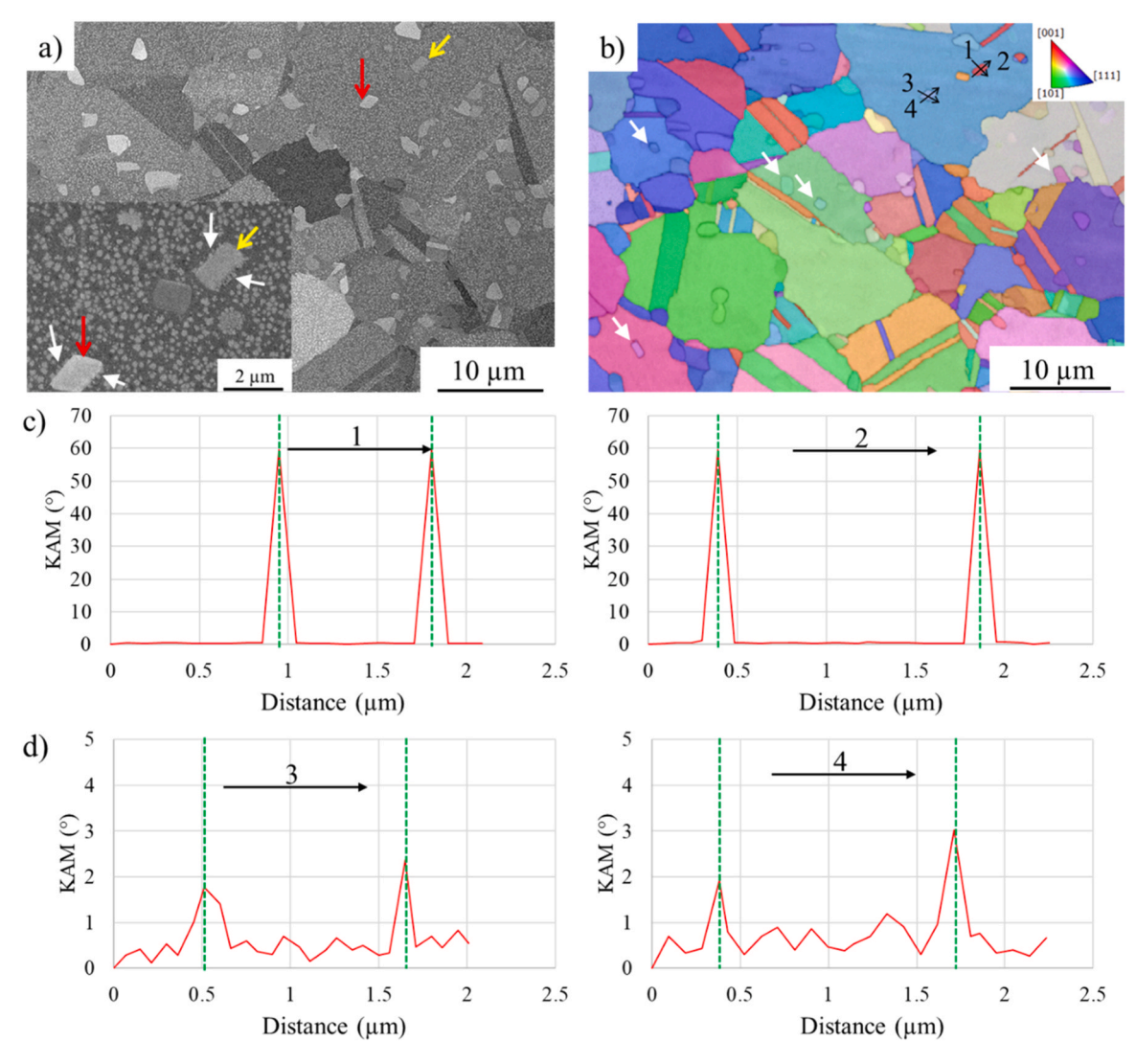


Fig. 4. SE image showing plate-like precipitates, and the inset presents a higher magnification view, where a T-type precipitate (indicated by the yellow arrow) and C-type precipitates (indicated by the red arrow) are highlighted. The protrusions of these precipitates are marked by white arrows in the inset image. (b) EBSD IPF map overlaid on the band contrast map, illustrating the orientation relationships in the region containing C/T-type precipitates; more plate-like precipitates are marked by white arrows in the inset. (c) Point-to-point misorientation profiles along directions 1 and 2 of the T-type precipitate. (d) Point-to-point misorientation profiles along directions 3 and 4 of the C-type precipitate.

To further confirm their alignment, SAED 1 and 8 were superimposed using Dragonfly software for [011] and [112] zone axes, as shown in Fig. 6m and l. A high-magnification view of the superimposed diffraction patterns was presented in Fig. 6n and o, highlighting the alignment between the precipitate and the matrix. The measured misorientation between these two diffraction patterns was approximately 0.1°, indicating a nearly perfect coherency between the phases. Moreover, the inter-planar spacing of the {111} plane of the precipitate (SAED 1) is the same as that of the matrix (SAED 6 and 8), with both exhibiting a value of 2.15 Å within the plate-like precipitate and 2.14 Å within the matrix. The lattice parameter can be calculated using Bragg's law as 3.72 Å and 3.72 Å in plate-like precipitate and matrix, respectively [52]. Since the diffraction patterns of the matrix and the precipitate are identical for two different zone axes ([011] and [112]) and both phases have FCC structure, the gamma and gamma prime are coherent, while it was shown in Fig. 5b-h that they are chemically different [53].

SAED 2, 3, and 4, all show the presence of additional diffraction spots associated with the twined region. The spot-type diffraction of SAED 2, 3, and 4 across the precipitate and matrix confirm that [011] is their shared zone axis, indicating the same orientations of the protrusions. SAED 5 reveals the diffraction features of both the matrix and the

protrusions, further supporting the alignment of their crystallographic structures.

A comparison of SAED 1, SAED 5, and SAED 8 shows that SAED 5 aligns with SAED 8, with no evidence of twinning diffraction. This indicates that the protrusions are aligned with the matrix rather than the precipitate. Even though the analysis primarily focused on matrix diffraction [50], SAED patterns 6, 7, and 8 present weaker superlattice diffraction features due to a lower volume fraction of the precipitate gamma prime phase when compared to SAED pattern 1.

To further clarify the crystallographic plane of the facet side of the precipitate at the interface, HR-TEM combined with Fast Fourier Transform (FFT) analysis was utilized, as shown in Fig. 7. Using DigitalMicrograph software, the area highlighted by the red square in Fig. 7a was magnified for detailed analysis in Fig. 7b, Fig. 7c–e display the FFT patterns obtained for the γ , γ/γ' interface, and γ' phases (indicated by the red solid square, red dotted square, and red dashed squares in Fig. 7b, respectively), allowing for precise identification of their interface without protrusions at their interface. For the FCC matrix phase, the diffraction reflections {131}, {111}, and {220} were identified. For the ordered L12 structure of the γ' phase, additional superlattice reflections, {021} and {110}, were observed in [112] zone axis in marked by the red

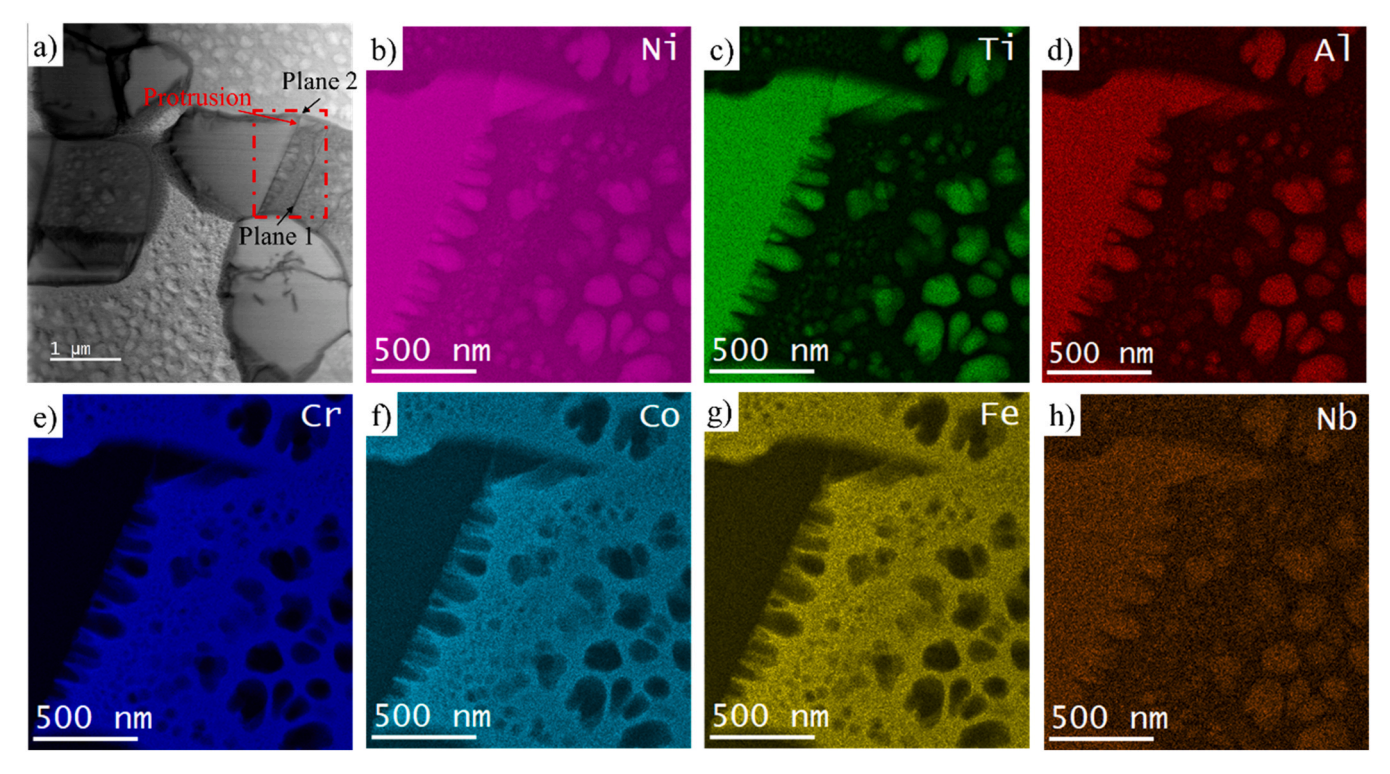


Fig. 5. (a) and (b) multi-beam image (JEOL-Bright field), (c-h) energy-dispersive X-ray spectroscopy (EDX) maps of a precipitate that has developed protrusions.

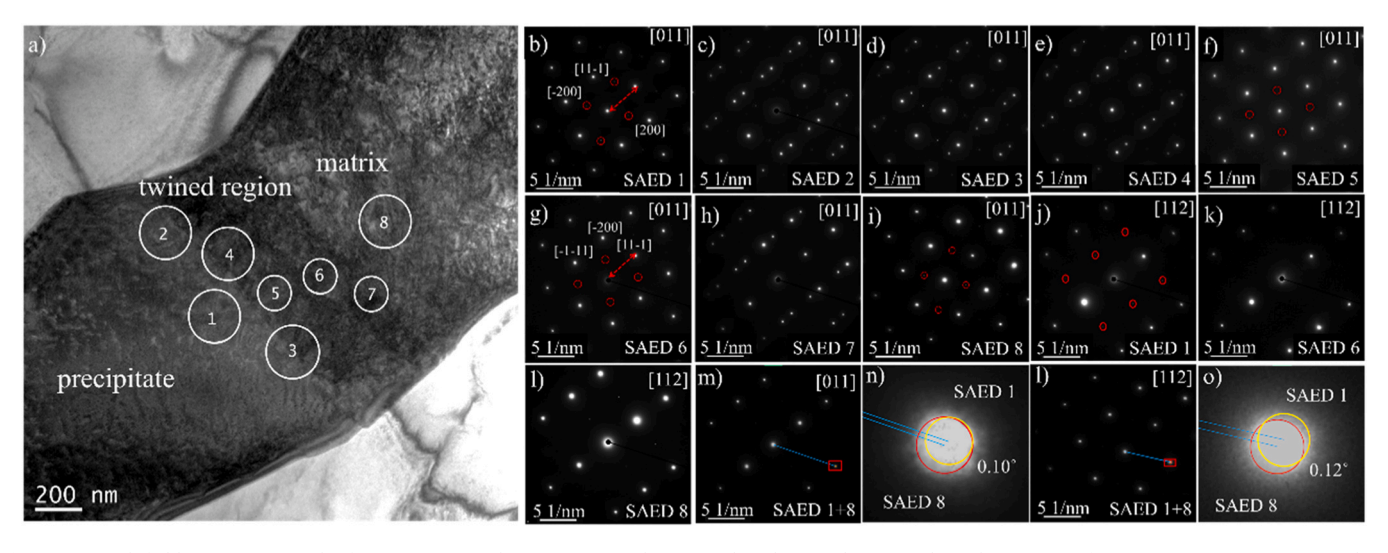


Fig. 6. (a) Dark-field TEM micrograph of a precipitate with protrusions and matrix. The white circles (1–8) show the positions for acquisition SAED patterns. (b–i) SAED of identified areas in (a) with [011] zone axis (red circles are superlattice spots originating from the gamma prime precipitates), (j–l) SAED of identified areas in (a) with [112] zone axis. The superimposed SAED patterns (SAED 1 and SAED 8) were obtained using Dragonfly software for (m and n) [011] and (l and o) [112] zone axes.

square in Fig. 7c [54].

Fig. 7f shows an HR-TEM image of γ' phase at higher magnification, enabling precise measurement of the interplanar spacing. The measured inter-planar spacing was found to be 2.15 Å, as shown in Fig. 7f. A comparison with SAED results from Fig. 6 confirmed that these planes correspond to the {111} planes on the γ' precipitate. Given their parallel alignment with the interface, it can be concluded that the {111} planes form the crystallographic plane of the facet side of the γ' precipitate. Considering the twin diffraction of the matrix at the interface in Figs. 6 and 7d, the habit plane between these two phases (the broad faces of the plate) is the {111} plane [52].

Using these findings, the lattice mismatch at the interface was

calculated by comparing atomic distances along the <100> direction of the facet side of the precipitate and the matrix, as shown schematically in Fig. 7g. γ' and γ phases were found to have identical inter-planar spacings of 2.15 Å and 2.14 Å for their (111) planes, corresponding to equivalent lattice parameters of 3.72 Å and 3.71 Å, respectively. If the adjacent phases share identical crystal structures and lattice parameters, any observed differences in lattice planes are expected to arise solely from compositional variations [24]. The calculated lattice misfit of 0.27 % falls within the range typically associated with a semi-coherent interface in Ni-based superalloys, as reported in multiple studies [17, 24].

Due to crystallographic misorientation between the precipitate and

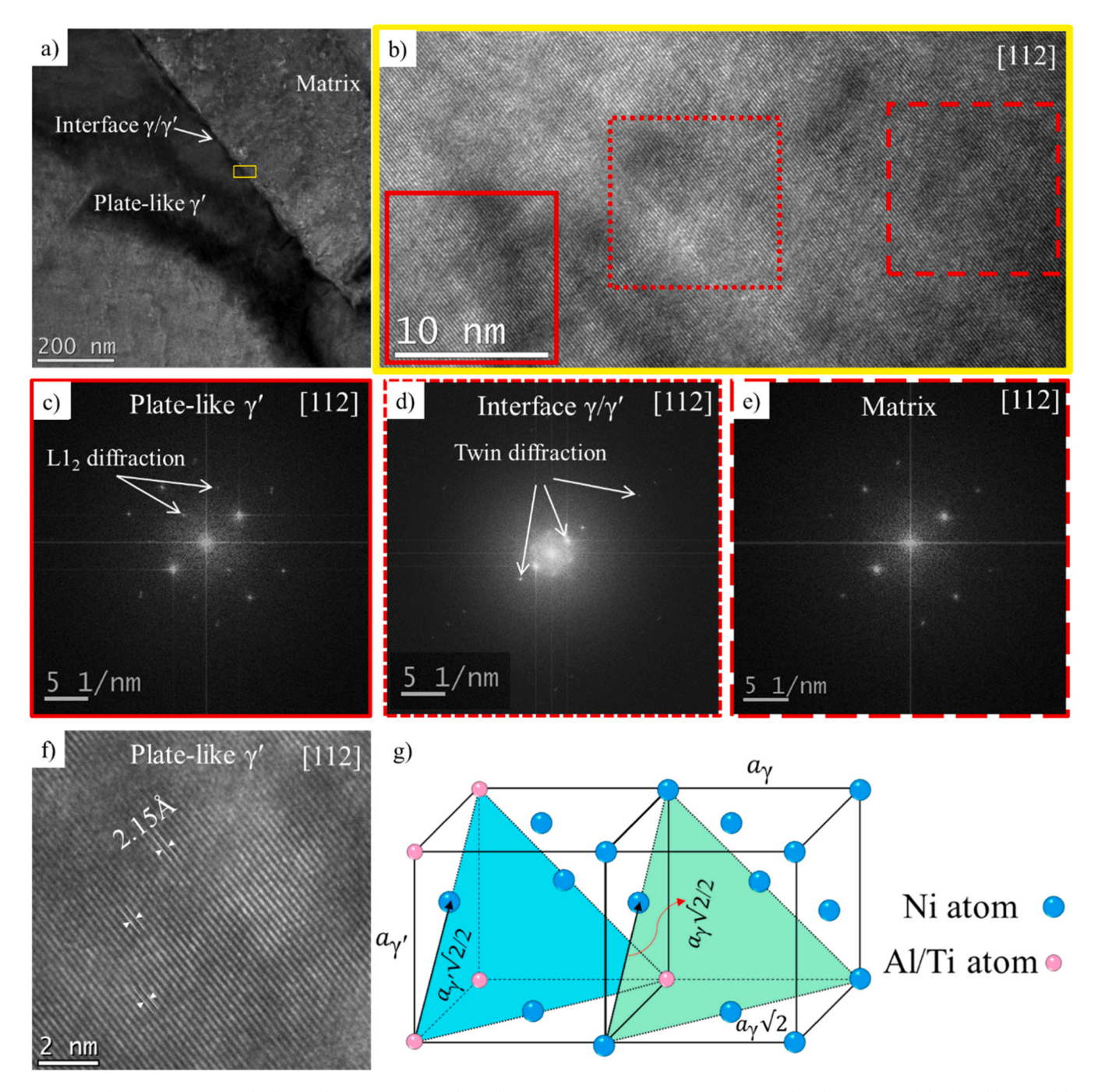


Fig. 7. (a) Multi-beam TEM image displaying the microstructure, (b) High-Resolution TEM (HR-TEM) image captured at the interface of the plate-like γ ' and the γ matrix, indicated by the yellow square in (a), (c) Fast Fourier Transform (FFT) pattern corresponding to plate-like γ ' (marked by the red square in (b)), (d) FFT pattern corresponding to the interface of γ/γ ' phase (marked by the doted red square in (b)), (e) and FFT pattern corresponding to the γ phase (marked by the red dashed square in (b)), (f) HR-TEM image of plate-like γ ', and (g) Schematic representation of the atomic arrangement at the interface between the plate-like γ ' phase and the γ matrix. The zone axis for both phases is [112] γ , γ .

the surrounding matrix, achieving atomic-resolution imaging at the interface using HR-TEM was technically challenging. Precise beam alignment parallel to the interface planes proved to be impossible technically, as it was not feasible to unambiguously determine whether the electron beam was positioned within the precipitate, a protrusion, or the matrix region during imaging. Consequently, in this study, the proposed dislocation-driven nucleation mechanism is based on the observed spatial correlation between protrusions and established dislocation behavior, as supported by prior literature.

3.2. Formation mechanism of the protruding interfaces

Two possible mechanisms could be envisaged for forming this type of protruding interface on the plate-like precipitates: 1) A dissolution-based mechanism or 2) a growth-based mechanism.

The first case assumes that the plate-like precipitates were already present in the microstructure of the as-received billet material [13]. Therefore, their facet-type interface could have evolved during the solution heat treatment at $1080~^{\circ}\text{C}$ due to the migration of atoms in the regions located in between the protrusions. In the second case, it is assumed that this interface type is formed due to the growth of a

'dendritic-like' feature, during the holding time and the cooling step [15]. Since the mechanism of interface migration can significantly influence the shape of second-phase particles [24,55], it is essential to examine both the plate-like precipitate/matrix interface and the protrusion/matrix interface. This examination will help determine the governing mechanism for the formation of the observed dendrite arm-like morphology. Concerning the first mechanism, some researchers [56,57] argue that the division of γ can be induced by the emergence of γ within the precipitates. As well, Xie et. al [58] found that dislocation cells and mechanical twins were formed in the interior of the matrix and primary γ '. Their interface would shift toward the inside of the precipitates along twin boundaries, resulting in the instability of their morphology [58]. In the present work, it was found that the plate-like precipitates had a twin-like interface or a few degrees of misorientation around an <111> axis relative to the matrix [32,33,37], therefore their interface should evolve by glissile transformation during dissolution, to preserve their specific orientation [55]. Taking into account boundary migration, Porter et al. [24] documented that the nearest neighbors of any atom are essentially unchanged during a glissile transformation; implying that the parent and product phases maintain identical compositions, and the transformation occurs without any diffusion. However, the EDX results, reported in Fig. 5b-h, show a clear difference between the chemical compositions of the plate-like precipitate and the matrix. Therefore, this suggests that the formation of the protrusions is not governed by a dissolution mechanism. Also, coherent twin boundaries, in which atoms fit perfectly into both phases, could be considered almost entirely immobile at temperatures even above 0.5 T_m (melting temperature) [24]. Furthermore, the denser packing of the special interfaces results in their lower mobility reducing the possibility that a dissolution-based mechanism could be at the origin of the formation of the dendritic-like interface in the present investigation.

A chemical analysis of the protrusions and their surrounding matrix is presented in Fig. 8. The image shows a cross-sectional FIB sample with a thickness of about 70 nm. The chemical analyses were done with EDX. Nine spots were analyzed across the interface perpendicular to the long axis of the protrusion (Fig. 8a). The results reported in Fig. 8b, show that while the matrix is predominantly composed of Cr and Co atoms, the precipitate is mainly composed of Ni, Al, Ti, and Nb with a distinct

variation of their chemical composition. It is noteworthy that at point number 3, which is located at the interface between the precipitate and the protrusion, the Ni, Ti, and Al concentrations decrease. This phenomenon is due to the 3D pear-shaped morphology of the protrusion. The term 'pear-shaped' describes the morphology of the protrusion, characterized by a narrowing near the precipitate-protrusion interface, a broadening toward the midsection of the protrusion, and a narrowing again as it approaches the tip. This shape is critical in controlling the chemical gradient observed, particularly the depletion and accumulation of elements at different points along the protrusion. Towards the midsection of the protrusion, the diameter of the protrusion increases, which brings changes in the chemical composition (e.g., spot 5 compared to spot 3). However, a clear change in chemical composition is observed when approaching the tip of the protrusion, as mentioned due to its morphology. Specifically, the chemical compositions of spots 5 and 6 are very different and the depletion of γ forming elements even extends about 50 nm into the matrix (spot 7). Taking into account the concentration of Ni as a key component in precipitates, there is a discernible upward gradient from the interface to the matrix (specifically, from spots 7–9). The concentrations of Co and Cr were decreasing as the main elements in the matrix from the tip of the protrusion towards

In the growth assumption, the matrix region adjacent to the interface becomes depleted of γ ' precipitating elements (Ni, Al, Nb, and Ti), and the concentration of these elements decreases below the bulk one [24] because there is a net transfer of solutes from the matrix to the precipitate [59]. Using the solution obtained from Fick's second law of diffusion in one dimension, two factors influence the diffusion rate between two neighboring phases during solid-state transformation: the diffusion coefficient and the concentration gradient. Although the diffusion coefficient should have the following sequence: Al> Cr> Co> Ti> Ni >Nb [40,41], the difference in concentration significantly affects their diffusion distance which leads to a lower diffusion of Nb, Ni, and Ti rather than Co and Cr. These findings are consistent with diffusion coefficient-based calculations (Table 1), which demonstrate the importance of Nb diffusion on the precipitate evolution [60]. Recently, Burlot et al. [49] also demonstrated that the precipitate-free zones (PFZs) development is governed volumetric diffusion of Nb in AD730 $^{\text{TM}}$. In

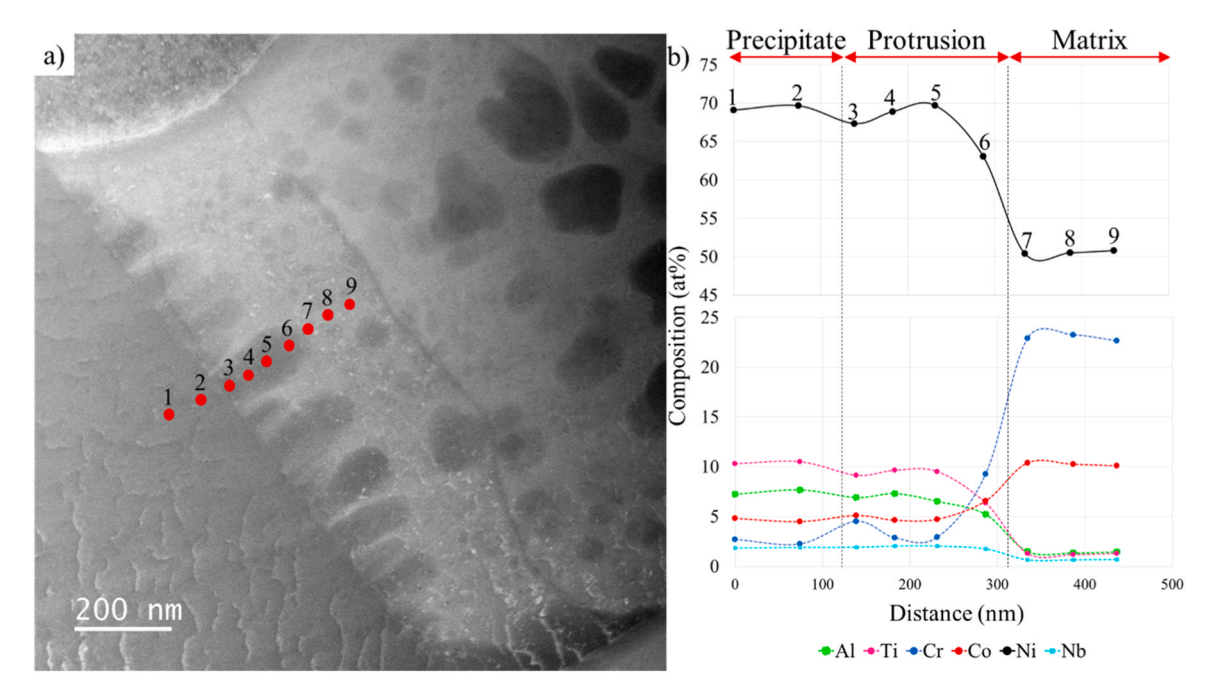


Fig. 8. (a) micrograph at the interface (analysis of chemical composition takes place at red spots), and (b) comparing Al, Ti, Nb, Ni, Cr, and Co concentration profiles between a plate-like γ , a protrusion, and a matrix based on spot analysis.

Table 1 Frequency factors (D_o), Activation energies (Q) [40,49,63], and calculated D of Nb, Ti, Ni, Co, Cr, and Al during solution heat treatment at 1080°C for 4 h in nickel.

	$D_0 (m^2/s)$	Q(kJ/mol)	D(m ² /s)
Nb	0.369×10^{-6}	232	4.1×10^{-16}
Ti	4.3×10^{-6}	257	5.1×10^{-16}
Ni	0.756×10^{-6}	237	5.4×10^{-16}
Co	$6.4 imes 10^{-6}$	250	1.4×10^{-15}
Cr	283×10^{-6}	276	$6.3 imes 10^{-15}$
Al	294×10^{-6}	269	1.2×10^{-14}

addition, it takes orders of magnitude longer for alloying elements to diffuse within the ordered precipitates than in the disordered phase [19]. So, the Al and Ti depletion is less than Ni depletion and Cr and Co enrichment at the interface [61]. Consequently, matrix areas adjacent to the γ - γ ' boundary might act as a barrier to diffusion, leading to diffusive interphase interfaces [19,62]. Therefore, the concentration of the major protrusion elements is expected to be depleted at the interface and then increase from the tip of the protrusions toward the matrix based on the proposed growth mechanism [15,59]. The above findings indicate that the protrusions have undergone a growth phase during relatively slow cooling, which has led to a depletion of the main precipitating elements in the matrix [15,24,59].

In addition, as shown in Fig. 8b, the concentrations of Ti, Al, and Ni increase with the distance from the protrusion tip towards the matrix. Considering the coherent/semi-coherent interface between this precipitate and the matrix, its growth could be considered interface-controlled [24]. The coherent/semi-coherent interfaces move as fast as the interface reaction progresses. Due to their lower mobility, the interface reaction will be driven by a higher chemical potential difference, resulting in a departure from the local equilibrium, therefore, the growth is controlled by the interface [24]. The above findings are in agreement with the findings reported by Link et al. [38] who also identified a growth mechanism responsible for groove formation during post-annealing cooling of SRR99 and CMSX-4 superalloys.

3.3. Protrusion's nucleation mechanisms

In the above sections, it was shown that protrusions were produced through a growth mechanism. Questions arise then on the nucleation mode, homogeneous or heterogeneous, the preferred nucleation sites [15], and its sequence during the cooling step. The second-phase particles nucleate homogeneously or heterogeneously throughout the matrix during the cooling step. The forming of a heterogeneous nucleus can lead to the elimination of a defect, resulting in the release of energy, and the activation energy barrier is thereby reduced or even eliminated [24]. Based on the appearance of the protrusions, their nucleation occurs heterogeneously with a low activation energy barrier, initiating at the interphase boundaries between the matrix and the plate-like precipitates under conditions of low undercooling [14]. In contrast, that of the secondary precipitates is homogeneous in the matrix at higher under-cooling. The extent of under-cooling serves as a critical determinant of nucleation sequence which confirms the chemical composition-based analysis.

The formation of protrusions at coherent/semi-coherent γ/γ interfaces is likely influenced by dislocations at the interface [64,65]. These dislocations typically arise during the solution heat treatment process, serving to relax interfacial misfit stresses. During the subsequent slow cooling phase, these dislocations can form regions of faster diffusion along the interface. The plausibility of this mechanism can be assessed by measuring the average distance between protrusions, which should correspond to the average dislocation spacing (d) required to relax the misfit. The theoretical dislocation spacing can be calculated using Brook's formula $d = b/\delta$, where b is the magnitude of the Burgers vector and δ is the lattice misfit [1,24,65].

By assuming that protrusions form on dislocations, the distance between the centers of each protrusion was measured to estimate the dislocation spacing. Multiple protrusions were analyzed in Fig. 5, and the average spacing between them was measured. Based on 20 measurements taken from the center of each protrusion, the average distance was determined to be $110 \text{ nm} \pm 10 \text{ nm}$. The reported uncertainty ($\pm 10 \text{ nm}$) corresponds to the standard deviation of the measurements, reflecting natural variations in dislocation spacing across the interface. Considering a 0.25 nm for the Burgers vector [1,65] and the dislocation spacing, the misfit would be 0.27 %. This value aligns well with the expected order of magnitude, supporting the hypothesis that dislocations play a critical role in the formation of these protrusions at semi-coherent interfaces.

Specifically, when AD730TM undergoes super-solvus solution treatment (eliminating primary gamma-prime particles) followed by holding at temperatures between 1030° C and 1080° C, intragranular cubic gamma-prime particles form [29,32]. This behavior qualitatively indicates a misfit magnitude exceeding 0.1 %. Such a significant misfit would be consistent with the formation of dislocations during heat treatment, facilitating the development of protrusions at the gamma/gamma-prime interface, as discussed above. Therefore, even without exact misfit values, the formation of these intragranular particles provides a qualitative indication of the substantial interfacial misfit in AD730TM.

However, in this context, the question arises as to why the plate-like precipitates are preferred sites for protrusion nucleation, but this is not the case for other precipitates, as well as primary γ ', secondary γ ', and tertiary γ ' (for example see Fig. 1).

By considering the protrusion formation mechanism described above and also the re-precipitation of dissolved elements during the cooling step, it can be said that there are not enough alloying elements for reprecipitation around the primary γ , and therefore, no protrusion could form at their interface [38,66]. Soares Janeiro et al. [66] reported that no dissolution of primary γ occurred even during sub-solvus hot deformation of Rene65 alloy, an alloy very similar to AD730TM, which supports the above interpretation. Furthermore, secondary and tertiary precipitates form coherently with the matrix [30] and there is no dislocation at this type of interface [24] therefore, protrusions could not be formed during the cooling step.

3.4. Nucleation sequence

The chemical composition of the primary γ , plate-like γ , secondary γ , and protrusion precipitates are given in Table 2. These results were obtained using EDX-TEM analysis of thin foil samples, about 70 nm thick, which is close to the thickness of the precipitates. Distinguishing the exact composition of the precipitates from the surrounding matrix becomes challenging when dealing with smaller precipitates, such as tertiary γ' . However, the analysis provides a good estimation of differences in composition [41]. The analysis of compositional variations among different precipitate types reveals significant disparities between the primary, secondary γ ', plate-like γ '-precipitates, and protrusions. In the secondary precipitates, characterized by their distinct morphology and distribution, concentrations of Ni, Al, Ti, and Nb are observed to be at their lowest, while conversely, those of Cr, Co, and Fe are at their highest. In contrast, the primary γ particles manifest a different compositional profile. As a result, Ni, Al, Ti, and Nb concentrations are higher, and Cr, Co, and Fe concentrations are lower, suggesting that these elements have a prominent role in the initial stages of precipitation [40,49]. The apparent reversal in concentration trends between the secondary precipitates and the other precipitate types underscores the complex interplay of alloying elements and microstructural evolution. These distinctions are indicative of the nucleation sequence governing their formation.

The compositional variation with precipitate size in the as-cooled microstructure exhibits similar composition-size relationships to those

Table 2 Chemical composition (wt%) of the matrix, primary γ ' [29], secondary γ ', plate-like γ ', and protrusion.

	Ni	Fe	Co	Cr	Mo	W	Al	Ti	Nb
Matrix	48.40 ± 0.04	5.54 ± 0.02	9.91 ± 0.02	19.60 ± 0.03	$\textbf{7.22} \pm \textbf{0.03}$	6.74 ± 0.03	0.70 ± 0.01	$\textbf{0.97} \pm \textbf{0.01}$	1.01 ± 0.01
Primary γ' [29]	73.00	1.5	5.00	3.30	0.40	0.40	4.60	10.30	0.40
plate-like γ'	71.03 ± 0.04	1.45 ± 0.01	4.79 ± 0.02	2.20 ± 0.01	1.90 ± 0.02	1.90 ± 0.02	3.38 ± 0.01	$\textbf{8.70} \pm \textbf{0.02}$	1.90 ± 0.02
Protrusion	69.11 ± 0.04	1.62 ± 0.01	4.87 ± 0.02	3.07 ± 0.01	2.54 ± 0.02	4.65 ± 0.03	3.20 ± 0.01	$\textbf{7.75} \pm \textbf{0.02}$	3.20 ± 0.02
Secondary γ'	67.26 ± 0.04	1.85 ± 0.01	5.00 ± 0.02	3.69 ± 0.01	3.15 ± 0.02	3.15 ± 0.03	$\textbf{3.24} \pm \textbf{0.01}$	$\textbf{7.43} \pm \textbf{0.02}$	3.15 ± 0.02

previously observed in this alloy. [40]. The process of supersaturation triggers the formation of secondary γ , in the initial cooling stages [14, 44]. As cooling progresses, these secondary precipitates grow until the limited diffusivity of the γ-stabilizing elements hinders their growth into the relatively larger (hundreds of nanometers) particles [67]. As a result, these elements are supersaturated within the matrix, starting the nucleation of additional intragranular second phases. At this point, the precipitates become tertiary, reaching sizes typically tens of nanometers in the subsequent cooling phases [40,41]. Studies by Masoumi et al. [40] indicate that the first population of γ is characterized by a higher content of Al and Ti, whereas secondary γ ' precipitates exhibit less Al and Ti content and increased concentrations of matrix elements such as Co and Cr compared to primary precipitates. The diffusion distances of the alloying elements in Ni are determined by their diffusion constants in the following order: Al>Cr>Co>Ni>Mo>W [68]. The restricted diffusion range of the γ-forming elements significantly contributes to the second-phase precipitation [68]. Hence, apart from particle dimensions. the chemical composition can also serve as a recognizable feature of different populations of precipitates in Ni-based superalloys with multiple precipitates [20]. Comparing the chemical composition of primary γ' , plate-like γ' , protrusions, and secondary γ' allows us to distinguish a sequence of precipitation. Subsequently, the protrusions initiate heterogeneous nucleation on the plate-like precipitates, which is driven by supersaturation of the matrix near the plate-like sites [20]. Ultimately, secondary γ ' nuclei form in the region supersaturated with Ni, Al, Nb, and Ti due to the higher undercooling.

3.5. Growth of protrusion

Based on Zener's model for the growth rate of precipitates [14] once nucleation is initiated, the saturation of γ moderately decreases, reducing the thermodynamic driving force for nucleation and subsequently slowing the growth rate, leading to a nearly constant proportion of the volume of the second phase in the matrix [44]. Nevertheless, with decreasing temperature, the repositioning of solute constituents becomes more challenging owing to the decreased diffusivity of elements. It was found that supersaturation alone is not the sole determinant of lack of stability. Nucleation densities and effective diffusivity within the second phases and matrix are also important items in γ ' growth [14]. Therefore, the surrounding matrix of plate-like γ is supersaturated due to the partial dissolution of this precipitates at solution temperature and holding time. By considering nucleation and growth of protrusions during cooling, the depletion of main elements limits the protrusion growth, resulting in their relatively smaller size rather than the secondary precipitates [55].

The formation of protrusions is anticipated to impact the mechanical behavior of superalloys during service conditions. It is well-documented that poly-crystalline Ni-base superalloys such as single-crystal Ni-based superalloys in aircraft engines experience non-isothermal conditions, such as overheating during takeoff. Subsequent cooling from these elevated temperatures to stable operating conditions can lead to the formation of protrusions [69–71]. This study provides insight into precipitate stability and morphological changes of precipitates in polycrystalline Ni-based superalloys. It allows the development of more accurate microstructure-based prediction models for predicting the lifetime of aerospace components.

While factors such as cooling rate, deformation history, and postheat treatment are well known to significantly influence the nucleation, growth, and coarsening behavior of primary, secondary, and tertiary γ' precipitates [14,20,32,72–76], their effect on the formation and evolution of plate-like γ' precipitates with dendrite arm-like interfaces remains unexplored. In this study, these unique precipitates were examined in the material immediately following solution treatment. Accordingly, the present work focuses on the detailed microstructural characterization of this novel type of γ' . Further investigations are required to systematically assess how processing variables influence the development and stability of these features.

4. Conclusions

In the present work, the presence of protrusions on plate-like precipitates was observed in a solution heat-treated AD730 $^{\rm TM}$ Ni-based superalloy. A combination of electron microscopy and analytical techniques, spanning from the micrometer to the atomic scale, was employed to characterize these features. While the findings are specific to AD730 $^{\rm TM}$, they may serve as a point of attention for researchers studying alloys, encouraging closer examination of such precipitate and matrix interfacial structures:

- 1) Plate-like γ' precipitates in statically recrystallized grains exhibit a lattice misfit of 0.27 %. These plate-like precipitates develop protrusions during air cooling from the solution temperature.
- 2) Analyzing the chemical composition of precipitates reveals a sequence of precipitation processes during air cooling. These begin with the heterogeneous nucleation of protrusions on plate-like precipitates, followed by secondary and tertiary nuclei in supersaturated regions.
- 3) The formation mechanisms of the protrusions were demonstrated to be of nucleation and growth type on dislocations at the interface of plate-like precipitates and matrix.

This study provides new insights into the formation and evolution of plate-like precipitates and their dendrite arm-like interfaces. Although numerous studies have demonstrated that interfacial characteristics significantly influence creep behavior and long-term performance, particularly through critical stress for Orowan bypass, shearing of γ' precipitates, and diffusion rate at the interface [19,23,77–81], this aspect was beyond the scope of the present study and has not been addressed here. This aspect was not addressed in the present work. Here, the focus was placed on characterizing the interface as comprehensively as possible. The potential effects of this specific morphology on mechanical behavior remain an open question and represent an important direction for future research, particularly in relation to post-processing conditions such as hot deformation, heat treatment, and welding.

CRediT authorship contribution statement

Mohammad Saadati: Writing – review & editing, Validation, Methodology, Formal analysis. **Jonathan Cormier:** Writing – review & editing, Validation, Investigation, Formal analysis. **Mohammad Jahazi:** Writing – review & editing, Validation, Supervision, Resources, Project administration, Funding acquisition, Conceptualization. **Parisa**

Darvishmotevally: Writing – review & editing, Writing – original draft, Visualization, Methodology, Investigation, Formal analysis, Conceptualization.

Declaration of Competing Interest

The authors declare the following financial interests/personal relationships which may be considered as potential competing interests: Parisa Darvishmotevally reports financial support was provided by Natural Sciences and Engineering Research Council of Canada. This research was funded by the Natural Sciences and Engineering Research Council of Canada (Grant number RGPIN 2018–03889). P.D. If there are other authors, they declare that they have no known competing financial interests or personal relationships that could have appeared to influence the work reported in this paper.

Acknowledgments

This research was funded by the Natural Sciences and Engineering Research Council of Canada (Grant number RGPIN 2018-03889). The authors would like to acknowledge Aubert & Duval Co. for providing the AD730™ samples. Special thank is extended to Dr. Jean-Philippe Masse for their invaluable discussions. Additionally, this work has been supported by technical data and characterization facilities from École de Technologie Supérieure (ÉTS) and Réseau Québécois de Microscopie Électronique des Matériaux (ROMEM).

References

- R.C. Reed, The Superalloys: Fundamentals and Applications, Cambridge University Press, New York, 2006
- [2] Y. Gai, R. Zhang, Z. Zhou, S. Lv, C. Cui, X. Xie, et al., Effect of c content on microstructure and hot deformation behavior of a Ni-based superalloy, J. Alloy. Compd. 965 (2023) 171453, https://doi.org/10.1016/j.jallcom.2023.171453.
- [3] A. Chamanfar, M. Jahazi, J. Cormier, A review on inertia and linear friction welding of Ni-based superalloys, Metall. Mater. Trans. A 46 (2015) 1639–1669, https://doi.org/10.1007/s11661-015-2752-4.
- [4] A. Harte, M. Atkinson, A. Smith, C. Drouven, S. Zaefferer, J. Quinta da Fonseca, et al., The effect of solid solution and gamma prime on the deformation modes in Nibased superalloys, Acta Mater. 194 (2020) 257–275, https://doi.org/10.1016/j.actamat.2020.04.004.
- [5] H. Ge, G. Liu, S. Zheng, Y. Yang, K. Liu, X. Ma, Dislocation climbing dominated decomposition and fracture of carbides in a Ni-based superalloy, Acta Mater. 246 (2023) 118669, https://doi.org/10.1016/j.actamat.2023.118669.
- [6] A. Jena, A.B. Gontcharov, P. Lowden, M. Brochu, Laser-direct energy deposition of the high \(\gamma \) LW 4280 Ni-based superalloy, J. Alloy. Compd. 1026 (2025) 180503, https://doi.org/10.1016/j.jallcom.2025.180503.
- [7] Y. Liu, B. Yin, P. Deng, T. Hu, C. Deng, M. Liu, et al., The effects of tensile stress on the microstructure evolution and elemental interdiffusion behavior of (Ni,Pt)Al coating and nickel-based superalloy at 1100 °C for 200h, J. Alloy. Compd. 946 (2023), https://doi.org/10.1016/j.jallcom.2023.169422.
- [8] D. Liu, R. Dong, X. Zhang, Y. Zhang, H. Hou, Y. Zhao, High-temperature oxidation behavior of Ni-Cr-W and Ni-Cr-Fe superalloys: a comparative study at 1000 °C, J. Alloy. Compd. 1025 (2025) 180271, https://doi.org/10.1016/j. iallcom.2025.180271.
- [9] F. Masoumi, L. Thébaud, D. Shahriari, M. Jahazi, J. Cormier, A. Devaux, et al., High temperature creep properties of a linear friction welded newly developed wrought Ni-based superalloy, Mater. Sci. Eng. A 710 (2018) 214–226, https://doi.org/ 10.1016/j.msea.2017.10.091.
- [10] M. Cottura, Y. Le Bouar, B. Appolaire, A. Finel, Rôle of elastic inhomogeneity in the development of cuboidal microstructures in Ni-based superalloys, Acta Mater. 94 (2015) 15–25, https://doi.org/10.1016/j.actamat.2015.04.034.
- [11] S. Tabaie, F. Rézaï-Aria, B.C.D. Flipo, M. Jahazi, Grain size and misorientation evolution in linear friction welding of additively manufactured IN718 to forged superalloy AD730TM, Mater. Charact. 171 (2021) 110766, https://doi.org/ 10.1016/j.matchar.2020.110766.
- [12] A. Nicolaÿ, G. Fiorucci, J.M. Franchet, J. Cormier, N. Bozzolo, Influence of strain rate on subsolvus dynamic and post-dynamic recrystallization kinetics of inconel 718, Acta Mater. 174 (2019) 406–417, https://doi.org/10.1016/j. actamat.2019.05.061.
- [13] A. Coyne-Grell, J. Blaizot, S. Rahimi, I. Violatos, S. Nouveau, C. Dumont, et al., Recrystallization mechanisms and associated microstructure evolution during billet conversion of a gamma-gamma' nickel based superalloy, J. Alloy. Compd. 916 (2022) 165465, https://doi.org/10.1016/j.jallcom.2022.165465.
- [14] F. Masoumi, D. Shahriari, M. Jahazi, J. Cormier, A. Devaux, Kinetics and mechanisms of γ' reprecipitation in a Ni-based superalloy, Sci. Rep. 6 (2016) 28650, https://doi.org/10.1038/srep28650.

- [15] R.A. Ricks, A.J. Porter, R.C. Ecob, The growth of γ' precipitates in Ni-based superalloys, Acta Met. 31 (1983) 43–53, https://doi.org/10.1016/0001-6160(83)
- [16] J. Coakley, D. Ma, M. Frost, D. Dye, D.N. Seidman, D.C. Dunand, et al., Lattice strain evolution and load partitioning during creep of a Ni-based superalloy single crystal with rafted γ' microstructure, Acta Mater. 135 (2017) 77–87, https://doi. org/10.1016/j.actamat.2017.06.021.
- [17] Y. Yamaguchi, R. Tajima, Y. Terada, morphology evolution of γ' precipitates for wrought Ni-based superalloys, Mater. Trans. 61 (2020) 2185–2194, https://doi. org/10.2320/matertrans.MT-MK2019003.
- [18] R.D. Doherty, Role of interfaces in kinetics of internal shape changes, Metall. Sci. 16 (1982) 367–374.
- [19] Y. Chen, R. Prasath Babu, T.J.A. Slater, M. Bai, R. Mitchell, O. Ciuca, et al., An investigation of diffusion-mediated cyclic coarsening and reversal coarsening in an advanced Ni-based superalloy, Acta Mater. 110 (2016) 295–305, https://doi.org/10.1016/j.actamat.2016.02.067.
- [20] W. Zhang, X. Liu, M. Zhu, Y. Guo, H. Qin, Q. Tian, Precipitation characteristics of γ precipitates of the GH4742 nickel-based superalloy at a slow cooling rate, J. Alloy. Compd. 941 (2023) 169013, https://doi.org/10.1016/j.jallcom.2023.169013.
- [21] R. Eriş, M.V. Akdeniz, A.O. Mekhrabov, Unveiling the effect of Hf-(Mo,W) addition on the coarsening, agglomeration, and dissolution behaviour of γ'-Ni₂Al precipitates in model Ni-based superalloys, J. Alloy. Compd. 936 (2023) 167869, https://doi.org/10.1016/j.iallcom.2022.167869.
- [22] X.Y. Li, H.P. Zhang, J.M. Bai, X.K. Li, J. Jia, C.S. Liu, et al., The evolution of γ' precipitates and hardness response of a novel PM Ni-based superalloy during thermal exposure, J. Alloy. Compd. 942 (2023) 168757, https://doi.org/10.1016/j.jallcom.2023.168757.
- [23] M. Durand, J. Cormier, F. Paumier, S. Katnagallu, A. Saksena, P. Kontis, et al., Chemical redistribution and change in crystal lattice parameters during stress relaxation annealing of the AD730TM superalloy, Acta Mater. 237 (2022) 118141, https://doi.org/10.1016/j.actamat.2022.118141.
- [24] D.A. Porter, K.E. Easterling, M.Y. Sherif, Phase Transformations in Metals and Alloys, CRC Press, Boca Raton, 2008.
- [25] Y. Wu, H. Zhao, J. Li, Y. Zhang, J. Liu, T. Liu, An innovative approach towards forming the serrated grain boundaries and refining the γ' precipitates in nickelbased superalloys, J. Alloy. Compd. 908 (2022) 164570, https://doi.org/10.1016/ j.jallcom.2022.164570.
- [26] L. Zhu, H. Pan, J. Cheng, L. Xiao, J. Guo, H. Ji, Dendrite evolution and quantitative characterization of \(\gamma\) precipitates in a powder metallurgy Ni-based superalloy by different cooling rates, J. Alloy. Compd. 918 (2022) 165677, https://doi.org/ 10.1016/j.jallcom.2022.165677.
- [27] B. Schulz, F. Theska, T. Leitner, M. Hafok, S. Primig, Discontinuous γ' nucleation due to boron and carbon segregation in Ni-based superalloys, J. Alloy. Compd. 1008 (2024) 176459, https://doi.org/10.1016/j.jallcom.2024.176459.
- [28] Y. Luo, C. Shi, H. Xu, Microstructure evolution and hot deformation characteristics of 15Cr-22Ni iron-base superalloy, J. Alloy. Compd. 938 (2023) 168628, https://doi.org/10.1016/i.iallcom.2022.168628.
- [29] S. Katnagallu, S. Vernier, M.A. Charpagne, B. Gault, N. Bozzolo, P. Kontis, Nucleation mechanism of hetero-epitaxial recrystallization in wrought nickel-based superalloys, Scr. Mater. 191 (2021) 7–11, https://doi.org/10.1016/j. scriptamat.2020.09.012.
- [30] M.A. Charpagne, T. Billot, J.M. Franchet, N. Bozzolo, Heteroepitaxial recrystallization: a new mechanism discovered in a polycrystalline γ-γ' nickelbased superalloy, J. Alloy. Compd. 688 (2016) 685–694, https://doi.org/10.1016/ i.iall.com/2016/07/240
- [31] P. Kontis, Z. Li, D.M. Collins, J. Cormier, D. Raabe, B. Gault, The effect of chromium and cobalt segregation at dislocations on nickel-based superalloys, Scr. Mater. 145 (2018) 76–80. https://doi.org/10.1016/j.scriptamat.2017.10.005.
- [32] S. Vernier, J.M. Franchet, C. Dumont, N. Bozzolo, A mechanism leading to γ' precipitates with {111} facets and unusual orientation relationships to the matrix in γ-γ' nickel-based superalloys, Metall. Mater. Trans. A 49 (2018) 4308–4323, https://doi.org/10.1007/s11661-018-4734-9.
- [33] S. Vernier, J.M. Franchet, C. Dumont, P. Vennéguès, N. Bozzolo, γ' precipitates with a twin orientation relationship to their hosting grain in a $\gamma-\gamma'$ nickel-based superalloy, Scr. Mater. 153 (2018) 10–13, https://doi.org/10.1016/j. scriptamat.2018.04.037.
- [34] Z.H. Wang, J.P. Xie, Q. Li, W.Y. Wang, A.Q. Wang, P. Liu, TiN/γ-Fe interface orientation relationship and formation mechanism of TiN precipitates in Mn18Cr2 steel, China Foundry 18 (2021) 180–184, https://doi.org/10.1007/s41230-021-9020-6
- [35] M. Saadati, R. Azari Khosroshahi, G. Ebrahimi, M. Jahazi, Twin-assisted precipitation during hot compression of an Mg-Gd-Zn-Zr magnesium alloy, Mater. Sci. Eng. A 706 (2017) 142–152, https://doi.org/10.1016/j.msea.2017.08.112.
- [36] F.J. Humphreys, M. Hatherly, Recrystallization and Related Annealing Phenomena, Elsevier Ltd, Kidlington, 2004.
- [37] S. Shanmugam, M. Peterlechner, M.R. Iskandar, U. Saikia, V. Kulitckii, M. Lipińska-Chwałek, et al., Coherent twin-oriented Al₃Sc-based precipitates in al matrix, Scr. Mater. 229 (2023) 115351, https://doi.org/10.1016/j.scriptamat.2023.115351.
- [38] T. Link, A. Epishin, M. Paulisch, T. May, Topography of semicoherent γ/γ' interfaces in superalloys: investigation of the formation mechanism, Mater. Sci. Eng. A 528 (2011) 6225–6234, https://doi.org/10.1016/j.msea.2011.04.049.
- [39] M. Huang, Z. Cheng, J. Xiong, J. Li, J. Hu, Z. Liu, et al., Coupling between re segregation and γ/γ interfacial dislocations during high-temperature, low-stress creep of a nickel-based single-crystal superalloy, Acta Mater. 76 (2014) 294–305, https://doi.org/10.1016/j.actamat.2014.05.033.

- [40] F. Masoumi, M. Jahazi, D. Shahriari, J. Cormier, Coarsening and dissolution of \(\gamma'\) precipitates during solution treatment of AD730TM Ni-based superalloy: mechanisms and kinetics models, J. Alloy. Compd. 658 (2016) 981–995, https://doi.org/10.1016/i.jallcom.2015.11.002.
- [41] Y.Q. Chen, E. Francis, J. Robson, M. Preuss, S.J. Haigh, Compositional variations for small-scale gamma prime (γ') precipitates formed at different cooling rates in an advanced Ni-based superalloy, Acta Mater. 85 (2015) 199–206, https://doi.org/ 10.1016/j.actamat.2014.11.009.
- [42] S. Tabaie, F. Rézaï-Aria, B.C.D. Flipo, M. Jahazi, Dissimilar linear friction welding of selective laser melted inconel 718 to forged Ni-based superalloy AD730TM: evolution of strengthening phases, J. Mater. Sci. Technol. 96 (2022) 248–261, https://doi.org/10.1016/j.jimst.2021.03.086.
- [43] A.R.P. Singh, S. Nag, S. Chattopadhyay, Y. Ren, J. Tiley, G.B. Viswanathan, et al., Mechanisms related to different generations of γ precipitation during continuous cooling of a nickel base superalloy, Acta Mater. 61 (2013) 280–293, https://doi. org/10.1016/j.actamat.2012.09.058.
- [44] S. Meher, S. Nag, J. Tiley, A. Goel, R. Banerjee, Coarsening kinetics of γ' precipitates in cobalt-base alloys, Acta Mater. 61 (2013) 4266–4276, https://doi.org/10.1016/j.actamat.2013.03.052.
- [45] Z. Li, H. Xie, F. Jia, Y. Lu, X. Yuan, S. Jiao, et al., Study on deformation characteristics and microstructure evolution of 2205/AH36 bimetal composite in a novel hot forming process, Metals 10 (2020) 1375, https://doi.org/10.3390/ met10101375
- [46] F. Theska, B. Schulz, M. Lison-Pick, S.R. Street, S. Primig, Precipitation-controlled grain boundary engineering in a cast and wrought Ni-based superalloy, J. Alloy. Compd. 1010 (2025) 177131, https://doi.org/10.1016/j.jallcom.2024.177131.
- [47] Y.Q. Zhang, G.Z. Quan, Y.Z. Yu, M.G. Quan, W. Xiong, Q. Jiang, et al., Workability improvement for hot forming process of Ni-38Cr-3.8Al superalloy by pre-ageing precipitation, J. Alloy. Compd. 1010 (2025) 178183, https://doi.org/10.1016/j.iallcom.2024.178183.
- [48] M.A. Charpagne, P. Vennéguès, T. Billot, J.M. Franchet, N. Bozzolo, Evidence of multimicrometric coherent γ' precipitates in a hot-forged γ-γ' nickel-based superalloy, J. Microsc. 263 (2016) 106–112, https://doi.org/10.1111/jmi.12380.
- [49] G. Burlot, J. Cormier, D. Eyidi, E. Cadel, P. Villechaise, Precipitate-free zones formation at grain boundaries in γ/γ Ni-based superalloys, J. Mater. Sci. (2024), https://doi.org/10.1007/s10853-024-09777-0.
- [50] J.R. Miller, J.F.S. Markanday, S.M. Fairclough, G.J. Wise, C.M.F. Rae, L.R. Owen, et al., Gamma prime precipitation in as-deposited Ni-based superalloy IN713LC, Scr. Mater. 239 (2024) 115775, https://doi.org/10.1016/j.scriptamat.2023.115775.
- [51] Ł. Rakoczy, M. Grudzień-Rakoczy, F. Hanning, G. Cempura, R. Cygan, J. Andersson, et al., Investigation of the γ precipitates dissolution in a Ni-based superalloy during stress-free short-term annealing at high homologous temperatures, Metall. Mater. Trans. A 52 (2021) 4767–4784, https://doi.org/ 10.1007/s11661-021-06420-4.
- [52] D.B. Williams, C.B. Carter, Transmission Electron Microscopy: A Textbook for Materials Science, Springer, Huntsville, AL, 2016.
- [53] J.Q. Wang, J.R. Wu, X.J. Guan, Y.S. Wu, S.H. Cheng, X.Z. Qin, et al., Tailoring microstructural stability and stress rupture properties of a solid-solution strengthened Fe-Ni-based superalloy via niobium addition, J. Alloy. Compd. 1008 (2024) 176628, https://doi.org/10.1016/j.jallcom.2024.176628.
- [54] Z. Tai, X. Wang, X. Zong, X. Ding, J. Liu, F. Kong, Microstructure and mechanical properties of an elevated temperature L1₂-type Ni-Co-Cr-Al-Ti-V-B-based highentropy intermetallic, J. Alloy. Compd. 1010 (2025) 177262, https://doi.org/ 10.1016/j.jallcom.2024.177262.
- [55] R. Sankaran, C. Laird, Kinetics of growth of platelike precipitates, Acta Met. 22 (1974) 957–969, https://doi.org/10.1016/0001-6160(74)90025-2.
- [56] F. Vogel, N. Wanderka, Z. Balogh, M. Ibrahim, P. Stender, G. Schmitz, et al., Mapping the evolution of hierarchical microstructures in a Ni-based superalloy, Nat. Commun. 4 (2013) 2955, https://doi.org/10.1038/ncomms3955.
- [57] V. Yardley, I. Povstugar, P.P. Choi, D. Raabe, A.B. Parsa, A. Kostka, et al., On local phase equilibria and the appearance of nanoparticles in the microstructure of single-crystal Ni-base superalloys, Adv. Eng. Mater. 18 (2016) 1556–1567, https:// doi.org/10.1002/adem.201600237.
- [58] X.F. Xie, J.L. Qu, J.H. Du, Z.N. Bi, Microstructure evolution characterization of Nibased GH4720Li superalloy during strain-controlled fatigue at 550 °C, J. Iron Steel Res. Int. 28 (2021) 901–909, https://doi.org/10.1007/s42243-020-00474-1.
- [59] H.B. Aaron, G.R. Kotler, second phase dissolution, Metall. Trans. 2 (1971) 393–408, https://doi.org/10.1007/BF02811639.
- [60] C.Y. Hung, S. Antonov, P.D. Jablonski, M. Detrois, Phase stability and phase transformation related to Nb/Ta additions in a Ni-based superalloy, J. Alloy. Compd. 952 (2023) 170071, https://doi.org/10.1016/j.jallcom.2023.170071.
- [61] J. Tiley, G.B. Viswanathan, R. Srinivasan, R. Banerjee, D.M. Dimiduk, H.L. Fraser, Coarsening kinetics of γ precipitates in the commercial nickel base superalloy rene 88DT, Acta Mater. 57 (2009) 2538–2549, https://doi.org/10.1016/j. actamat.2009.02.028.

- [62] S. Zhao, Y. Osetsky, Structural and chemical disorder enhance point defect diffusion and atomic transport in Ni_aAl-based γ' phase, Acta Mater. 207 (2021) 116704, https://doi.org/10.1016/j.actamat.2021.116704.
- [63] X. Zhang, H. Deng, S. Xiao, Z. Zhang, J. Tang, L. Deng, et al., Diffusion of co, ru and re in Ni-based superalloys: a first-principles study, J. Alloy. Compd. 588 (2014) 163–169, https://doi.org/10.1016/j.jallcom.2013.11.024.
- [64] J.C. Zhu, Y.C. Lin, Z.J. Chen, S.X. Li, D.G. He, Y.L. Qiu, et al., Interaction mechanism between primary γ' precipitate and dislocation of nickel-based P/M superalloy: incoherent primary γ' precipitate trap, J. Alloy. Compd. 1021 (2025) 179732, https://doi.org/10.1016/j.jallcom.2025.179732.
- [65] L. Dirand, J. Cormier, A. Jacques, J.P. Chateau-Cornu, T. Schenk, O. Ferry, et al., Measurement of the effective γ/γ' lattice mismatch during high temperature creep of Ni-based single crystal superalloy, Mater. Charact. 77 (2013) 32–46, https://doi. org/10.1016/j.matchar.2012.12.003.
- [66] I. Soares Janeiro, J.M. Franchet, J. Cormier, N. Bozzolo, Dynamic precipitation during forging of a γ - γ nickel-based superalloy, Metall. Mater. Trans. A 54 (2023) 2052–2070, https://doi.org/10.1007/s11661-023-06996-z.
- [67] W. Xia, X. Zhao, J. Wang, Q. Yue, Y. Cheng, L. Kong, et al., New strategy to improve the overall performance of single-crystal superalloys by designing a bimodal γ' precipitation microstructure, Acta Mater. 257 (2023) 119200, https://doi.org/ 10.1016/j.actamat.2023.119200.
- [68] P. Qu, W. Yang, J. Qin, C. Liu, K. Cao, J. Zhang, et al., Precipitation behavior and chemical composition of secondary γ precipitates in a Re-containing Ni-based single crystal superalloy, Intermetallics 119 (2020) 106725, https://doi.org/ 10.1016/j.intermet.2020.106725.
- [69] J. Rame, D. Eyidi, A. Joulain, M. Gauthé, J. Cormier, Creep and tensile behavior of a nickel-based single crystal superalloy with a bimodal y precipitation, Metall. Mater. Trans. A 54 (2023) 1496–1508, https://doi.org/10.1007/s11661-023-07022-y
- [70] J. Cormier, X. Milhet, J. Mendez, Non-isothermal creep at very high temperature of the nickel-based single crystal superalloy MC2, Acta Mater. 55 (2007) 6250–6259, https://doi.org/10.1016/j.actamat.2007.07.048.
- [71] R. Giraud, Z. Hervier, J. Cormier, G. Saint-Martin, F. Hamon, X. Milhet, et al., Strain effect on the \(\) dissolution at high temperatures of a nickel-based single crystal superalloy, Metall. Mater. Trans. A 44 (2013) 131–146, https://doi.org/ 10.1007/s11661-012-1397-9.
- [72] S.S. Babu, M.K. Miller, J.M. Vitek, S.A. David, Characterization of the microstructure evolution in a nickel base superalloy during continuous cooling condition, Acta Mater. 49 (2001) 4149–4160, https://doi.org/10.1016/S1359-6454(01)00294-1.
- [73] A.R.P. Singh, S. Nag, S. Chattopadhyay, Y. Ren, J. Tiley, G.B. Viswanathan, et al., Mechanisms related to different generations of γ' precipitation during continuous cooling of a nickel base superalloy, Acta Mater. 61 (2013) 280–293, https://doi.org/10.1016/j.actamat.2012.09.058.
- [74] S. Tabaie, F. Rézaï-Aria, B.C.D. Flipo, J. Cormier, M. Jahazi, Post-weld heat treatment of additively manufactured inconel 718 welded to forged Ni-based superalloy AD730 by linear friction welding, Metall. Mater. Trans. A 52 (2021) 3475–3488. https://doi.org/10.1007/s11661-021-06319-0.
- [75] L.O. Osoba, A.K. Khan, S.O. Adeosun, Cracking susceptibility after post-weld heat treatment in haynes 282 nickel-based superalloy, Acta Metall. Sin. (Engl. Lett.) 26 (2013) 747–753, https://doi.org/10.1007/s40195-013-0252-3.
- [76] L. Huang, Z. Fu, C. Chu, W. Chen, H. Wang, D. Zhu, Microstructure and mechanical behavior in a spherical L1₂ nanoprecipitates strengthened Ni35Co27.5Cr27.5Al5Ti5 high-entropy alloy fabricated by direct casting and heat treatment, J. Alloy. Compd. 1002 (2024) 175299, https://doi.org/10.1016/j. jallcom.2024.175299.
- [77] J.C. Guo, S.X. Han, R.N. Yang, X.W. Lei, N. Wang, Influence of γ/γ morphology evolution on the mechanical properties of Ni-based single crystal superalloys formed by laser metal deposition, Mater. Sci. Eng. A 836 (2022) 142714, https:// doi.org/10.1016/j.msea.2022.142714.
- [78] L. Dirand, J. Cormier, A. Jacques, J.P. Chateau-Cornu, T. Schenk, O. Ferry, et al., Measurement of the effective γ/γ lattice mismatch during high temperature creep of Ni-based single crystal superalloy, Mater. Charact. 77 (2013) 32–46, https://doi. org/10.1016/j.matchar.2012.12.003.
- [79] H. Fan, H. Long, J. Zhao, X. Yuan, Y. Zhao, Y. Liu, et al., Effect of γ' size on the high-temperature low-stress creep life of nickel-based single-crystal superalloys, SSRN Electron. J. (2024), https://doi.org/10.2139/ssrn.4958558.
- [80] Y. Ru, S. Li, J. Zhou, Y. Pei, H. Wang, S. Gong, et al., Dislocation network with pair-coupling structure in {111} γ/γ interface of Ni-based single crystal superalloy, Sci. Rep. 6 (2016) 29941, https://doi.org/10.1038/srep29941.
- [81] R. Giraud, Z. Hervier, J. Cormier, G. Saint-Martin, F. Hamon, X. Milhet, et al., Strain effect on the \(\) dissolution at high temperatures of a nickel-based single crystal superalloy, Metall. Mater. Trans. A 44 (2013) 131–146, https://doi.org/ 10.1007/s11661-012-1397-9.